JGR Solid Earth

RESEARCH ARTICLE
10.1029/2021JB022329

Constraints on Mantle Viscosity From Slab Dynamics

Hao Liu[1,2,3], **Michael Gurnis**[3], **and Wei Leng**[1,2]

[1]Laboratory of Seismology and Physics of Earth's Interior, School of Earth and Space Sciences, University of Science and Technology of China, Hefei, China, [2]CAS Center for Excellence in Comparative Planetology, Hefei, China, [3]Seismological Laboratory, California Institute of Technology, Pasadena, CA, USA

Key Points:

- A low viscosity channel (LVC) between 660 and 1,000 km lowers the geoid over slabs
- The LVC increases downdip tension in the upper 300 km within slabs
- Our results favor viscous models without the presence of the LVC

Supporting Information:

Supporting Information may be found in the online version of this article.

Correspondence to:

H. Liu,
liuhao@caltech.edu

Citation:

Liu, H., Gurnis, M., & Leng, W. (2021). Constraints on mantle viscosity from slab dynamics. *Journal of Geophysical Research: Solid Earth*, *126*, e2021JB022329. https://doi.org/10.1029/2021JB022329

Received 29 APR 2021
Accepted 11 JUL 2021

Abstract The radial viscosity of the mantle is generally thought to increase by ~10–100 times from the upper to lower mantle with a putative, abrupt increase at 660 km depth. Recently, a low viscosity channel (LVC) between 660 and 1,000 km has been suggested. We conduct a series of time-dependent flow models with viscosity either increasing or decreasing at 660 km depth while tracking slab structure, state-of-stress, and geoid. We find that a LVC will lower the amplitude of long wavelength (>5,000 km) geoid highs over slabs, with amplitudes <10 m in height, while increasing the slab dip angle and downdip tension in the upper 300 km of slabs. A viscosity increase at 660 km gives rise to strong downdip compression throughout a slab and this pattern will largely go away with the introduction of the LVC. In addition, the endothermic phase change at 660 km depth can substantially affect the stress distribution within slabs but has a minor influence on the geoid. Models that fit the observed long wavelength geoid and observed focal mechanism in the western Pacific favor models without the presence of the LVC between 660 km and 1,000 km depths.

Plain Language Summary The viscosity of the mantle plays a key role in the thermochemical evolution of the Earth. It is generally believed that the mantle has a viscosity jump of 10–100 times at 660 km depth. Recently, some scholars suggest that there is a low viscosity channel (LVC) between 660 and 1,000 km depths. Here, we developed a series of geodynamic models with viscosity either increasing or decreasing at 660 km depth to track slab structure, state-of-stress, and geoid. We find that the existence of the LVC will reduce the amplitude of long wavelength geoid (>5,000 km) over slabs to less than 10 m, and increase the slab dip angle and downdip tension in the upper 300 km of slabs. An increase in viscosity at 660 km will lead to strong downdip compression throughout a slab, however, this pattern will disappear with the introduction of the LVC. In addition, the postspinel phase transition has a large influence on the stress state within slabs, but has a minor influence on the geoid. Compared with the observed long wavelength geoid and focal mechanism in the western Pacific, our models do not support the existence of the LVC between 660 and 1,000 km depths.

1. Introduction

The radial viscosity structure of Earth's mantle plays a key role in the transport of heat and mass by convection, especially the ascent of plumes and the descent of subducted slabs between the upper and lower mantle (Agrusta et al., 2017; Ballmer et al., 2015; Goes et al., 2017; Homrighausen et al., 2020; Li et al., 2019). Different radial viscosity profiles of the mantle have been proposed using the results of laboratory experiments (Hirth & Kohlstedf, 2003), through inversion of glacial isostatic adjustment data (GIA) or inversion of the long wavelength geoid (Forte et al., 2015; King, 1995; Mitrovica & Forte, 2004). Microphysical models of mantle viscosity strongly depend on grain size, activation volume and activation energy, and their extrapolation to mantle conditions relies on experimentally determined parameters, some of which are poorly constrained (Hirth & Kohlstedf, 2003; Karato, 2008). GIA processes occurring over millennial timescales (with associated sea level variations, changes in the gravitational field and Earth rotation) are sensitive to the radial distribution of mantle viscosity (Forte et al., 2015; Mitrovica & Forte, 2004). Over much longer timescales (million years), the mantle viscosity plays a significant role in the thermochemical evolution of Earth's interior (Forte et al., 2015; King, 1995, 2016).

Although the characteristics of inferred mantle viscosity depend on seismic tomographic models, seismic velocity to density scalings, geodynamic data (e.g., geoid, dynamic topography), and inversion approaches (e.g., Monte-Carlo, genetic algorithms), it is generally argued that the radial viscosity profile has an increase

of ∼10–100 times at 660 km depth. A compelling argument for such an increase has been made from the long wavelength geoid and the state-of-stress within slabs (as constrained from seismic centroid moment tensor solutions) (e.g., Alpert et al., 2010; Hager & Richards, 1989; King & Masters, 1992; Richards & Hager, 1984; Vassiliou et al., 1984). Alternatively, a thin weak layer beneath the mantle transition zone has been proposed based on the joint inversion of GIA and mantle flow models (e.g., Mitrovica & Forte, 2004) possibly due to the existence of grain size reduction (Panasyuk & Hager, 1998). Such viscosity structures have important implications for mantle convection. For example, the viscosity increase at 660 km depth will strongly influence the width of plumes as they ascend from the lower to upper mantle and the degree of slab deformation within the mantle transition zone (Goes et al., 2017; Leng & Gurnis, 2012; Li et al., 2019). A thin low viscosity layer beneath the mantle transition zone could promote the generation of horizontal slabs within the mantle transition zone (Mao & Zhong, 2018). A key observation is the horizontal slab in the mantle transition zone below east Asia and Mao and Zhong (2018) have argued that this structure is well matched by models with a decrease in viscosity at 660 km depth, while Ma et al. (2019) have argued that a better fit is obtained with a traditional increase in viscosity at 660 km depth if updated plate reconstructions are used. In addition, when a thin weak layer and weak asthenosphere are incorporated into a 3-D geodynamic model in a spherical geometry, plumes with a tree-like structure will form. Such a structure is consistent with recent high-resolution tomographic results (e.g., the western Indian Ocean plume cluster and Tristan mantle plume) derived from ocean bottom seismograph (OBS) (Liu & Leng, 2020).

In flow models that fit the long wavelength geoid, a low viscosity channel between 660 km and 1,000 km depths has been suggested through inversion without a priori layered structures (Rudolph et al., 2015), consistent with previous inversions with a prescribed layered viscosity (Forte & Peltier, 1991; Kido et al., 1998; King & Masters, 1992). Such a viscosity structure with a jump at ∼1,000 km depth can potentially explain the long wavelength geoid (spherical harmonic degrees 2–7) and the interpretation of seismic images, such as slab orphaning, slab stagnation, and plume deflection at 1,000 km depth (Grima et al., 2020; Rudolph et al., 2015). In contrast, using a thermochemical convection model, Liu and Zhong (2016) argue that a mantle with an increase in viscosity at 660 km discontinuity better fits the observed geoid than a model with an increase at 1,000 km depth. Thus, distinguishing between viscosity structures at 660 km deserves further consideration.

A number of studies have addressed the origin of geoid highs associated with subducted slabs and the constraints which can be placed on mantle viscosity variations from such models (e.g., Hager, 1984; Moresi & Gurnis, 1996; Yoshida & Nakakuki, 2009). Richards and Hager (1989) suggest that lateral viscosity variations derived from temperature anomalies would have negligible influence on the geoid at the longest wavelength (spherical harmonic degrees 2 and 3) but would produce prominent contamination in degree 4 and above. Zhang and Christensen (1993) further confirm this implication based on the combination of a dynamic model and tomography models. However, with a suite of 3-D regional models, Moresi and Gurnis (1996) showed that the geoid is sensitive to lateral viscosity variations induced by slabs. Some mantle flow models with stiff slabs and weak plate margins yield a good fit to the observed geoid (e.g., Ghosh et al., 2010; Tosi et al., 2009; Yoshida & Nakakuki, 2009; Zhong & Davies, 1999).

In addition to the geoid height argument over slabs, an important constraint on mantle viscosity comes from the focal mechanism of earthquakes within slabs (e.g., Alpert et al., 2010; Vassiliou et al., 1984). Numerical models of subduction zones that fit the stress orientations of intermediate and deep focus earthquakes require a viscosity increase of at least 10 times at 660 km depth (Vassiliou et al., 1984). Besides, self-consistent subducting slab models, consistent with the stress state and morphology of slabs further support an increase of at least 10–30 times from the upper to the lower mantle (Gurnis & Hager, 1988). Moreover, when strain rates and stress orientations inferred from global seismicity are compared to modeled deformations, the maximum viscosity of slabs must be less than 3×10^{23} Pa·s and the lower mantle must be ∼30–100 times more viscous than the upper mantle (Alpert et al., 2010; Billen et al., 2003). The majority of continuous slabs are more likely to be dominated by downdip compression throughout, especially western Pacific subduction zones such as the Kurile, Izu-Bonin, and Tonga-Kermadec slabs (Figure 1) while some slabs show that downdip tension dominates in the upper 300 km, such as Peru and Chile (e.g., Alpert et al., 2010; Isacks & Molnar, 1971). Thus, we conduct a series of geodynamic models to investigate the effects of the competing

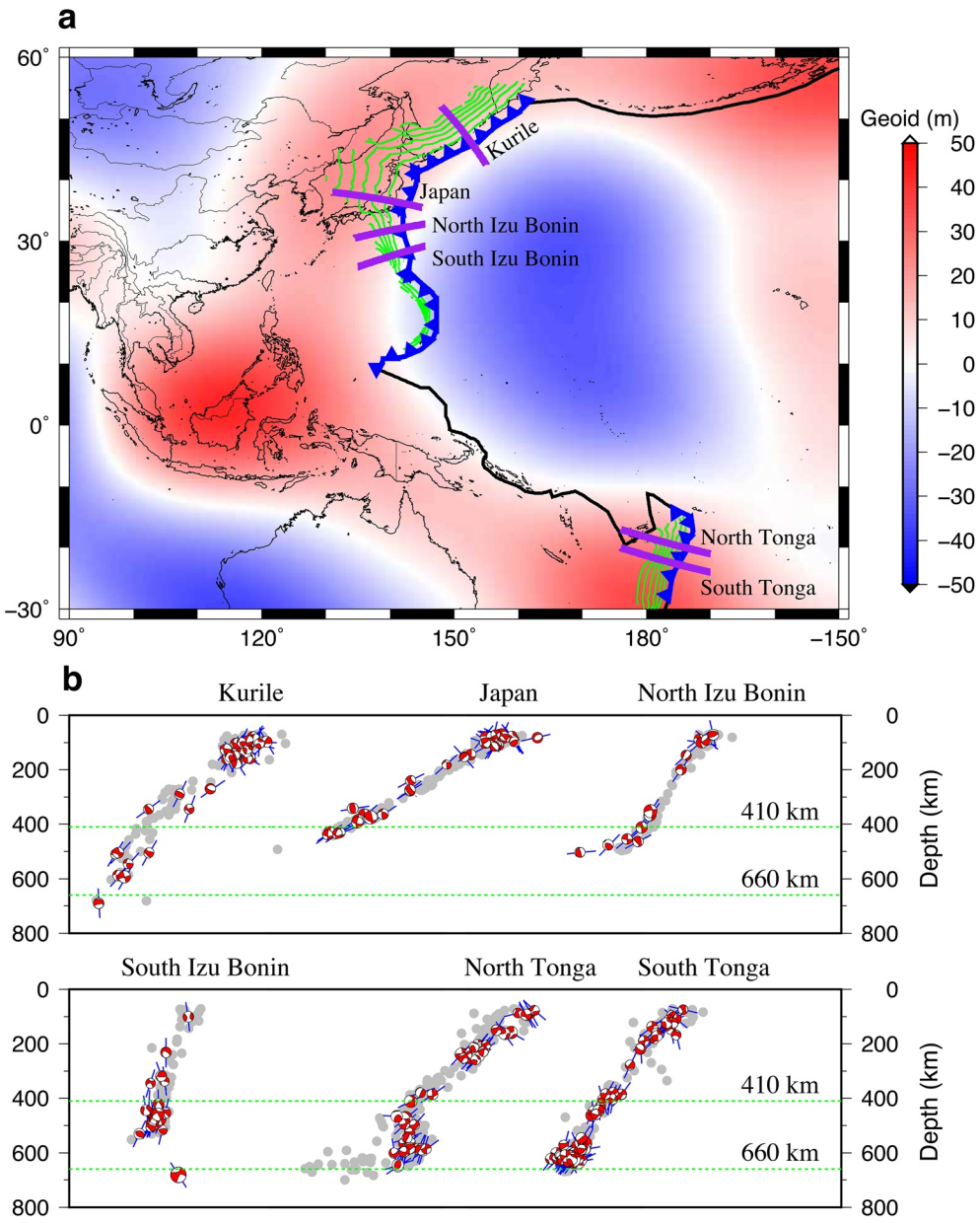

Figure 1. (a) Global long wavelength geoid (the degrees 4–12) from EGM96 (Lemoine et al., 1997). Green curved lines represent slab interface depth from Slab 1.0 model (Hayes et al., 2012), bold black line and blue lines show the Pacific plate boundary and trench locations, respectively. (b) Deep earthquake distributions and focal mechanisms along different profiles (purple lines) in (a). Gray circles represent deep earthquakes from the EHB catalog (Engdahl et al., 1998). Beach balls show global centroid moment tensor (CMT) focal mechanisms. Blue lines represent the orientations of the compressional (*P*) axes of the CMT solutions.

mantle viscosity structures on slab dynamics (in terms of the geoid and state-of-stress). We attempt to find those viscosity structures (and mantle phase transitions) most consistent with observations.

2. Method

We compute time-dependent viscous (Stokes) flow while making the Boussinesq approximation and assuming incompressibility in a 2-D Cartesian geometry with the finite element method. The nondimensional governing equations are solved with the Citcom software (Moresi et al., 1996). The model domain is

5,780 km horizontally (X direction) with 832 linear elements and 2,890 km in depth (Z) with 192 elements. With mesh refinement, the radial element size increases gradually from ~5 to ~39 km from the uppermost mantle to the lowermost mantle.

The trench is initially located at 3,800 km in the X direction and serves as a division between a subducting and overriding plate, which have lithospheric ages of 100 and 20 Myr, respectively (Figure 2a). The initial temperature is described by a half-space cooling model (Turcotte & Schubert, 2014). The nondimensional mantle viscosity is described as a composite between diffusion and dislocation creep and depends on temperature, strain rate, and depth (McNamara et al., 2001; Yang et al., 2017; Zhong & Gurnis, 1995):

$$\eta = \frac{\eta_{dif}\eta_{dis}}{\eta_{dif} + \eta_{dis}}, \tag{1}$$

where η is the effective viscosity; η_{dif} and η_{dis} are the viscosity arising from diffusion and dislocation deformation, respectively, and expressed as:

$$\eta_{dif} = \eta_0 \exp\left[E_0\left(T_0 - T\right) + 1.433 + 11.753Z - 14.235Z^2\right], \tag{2}$$

$$\eta_{dis} = \left(\frac{\dot{\varepsilon}_0}{\dot{\varepsilon}_{II}}\right)^{1-1/n} \eta_{dif}^{\,1/n}, \tag{3}$$

where η_0, E_0, T_0, T, and Z are the reference viscosity in the asthenosphere, the activation energy, reference temperature, temperature, and depth; $\dot{\varepsilon}_0$, $\dot{\varepsilon}_{II}$, and n represent the reference strain rate, square root of the second invariant of strain rate tensor, and nonlinear exponent for dislocation creep, respectively. The mantle radial viscosity profile in diffusion creep was based on previous inferences from a joint inversion of mantle convection and postglacial isostatic adjustment data (Mitrovica & Forte, 2004). In addition, we use a weak-zone stencil ψ to decouple the subducting and overriding plates expressed as:

$$\psi = \Gamma\left(|x| - \lambda_x, \mu_x\right) \times \Gamma\left(z - \lambda_z, \mu_z\right), \tag{4}$$

$$\Gamma\left(d, \mu\right) = 0.5\left(1 - \tanh\left(\frac{d}{\mu}\right)\right), \tag{5}$$

where λ is a length scale that defines the lateral and depth extent of the stencil and μ controls the smoothing within stencil. The stencil ranges from 0 for ambient mantle to 1 for the weak zone, which is incorporated into viscosity by $\eta = \eta\exp\left(\psi k\right)$, where k is a constant controlling the viscosity of the weak-zone stencil (Bower et al., 2015; Yang et al., 2017). The influence of a LVC on slab dynamics is investigated with three kinds of viscosity structures, one which increases at 660 km depth (Figure 2c), one decreasing in viscosity at 660 km depth (Figure 2d), and one increasing in viscosity at 1,000 km depth (Figure 2e). The maximum viscosity (1.5×10^{24} Pa·s) and minimum viscosity (9.0×10^{18} Pa·s, the viscosity of the weak-zone stencil) are imposed. All related parameters can be found in Tables 1 and 2.

Furthermore, phase transitions, represented by a phase change function (Christensen & Yuen, 1985; Liu et al., 2018; Schmeling et al., 1999; Yang et al., 2018), from olivine to wadsleyite at 410 km depth, metastable olivine, and ringwoodite to bridgemanite and magnesiowüstite (postspinel phase change) at 660 km depth are incorporated. We primarily explore the effects of the postspinel phase change on the stress state within the slab and the geoid over slab. A more complicated set of phase change functions could be used (Billen, 2020), but our objective is to focus on the first-order influence of the mantle phase transitions.

In addition, we also use self-consistent models in which plate kinematics are an outcome (Moresi et al., 1996; Zhong, 2006) to further understand the effects of different viscosity structures on slab dynamics. Our model domain is 6,000 km horizontally (X direction) with 832 linear elements and 2,000 km in depth (Z) with 192 elements. In the vertical direction, element size changes from ~3 to ~28 km from the uppermost mantle to the lowermost mantle.

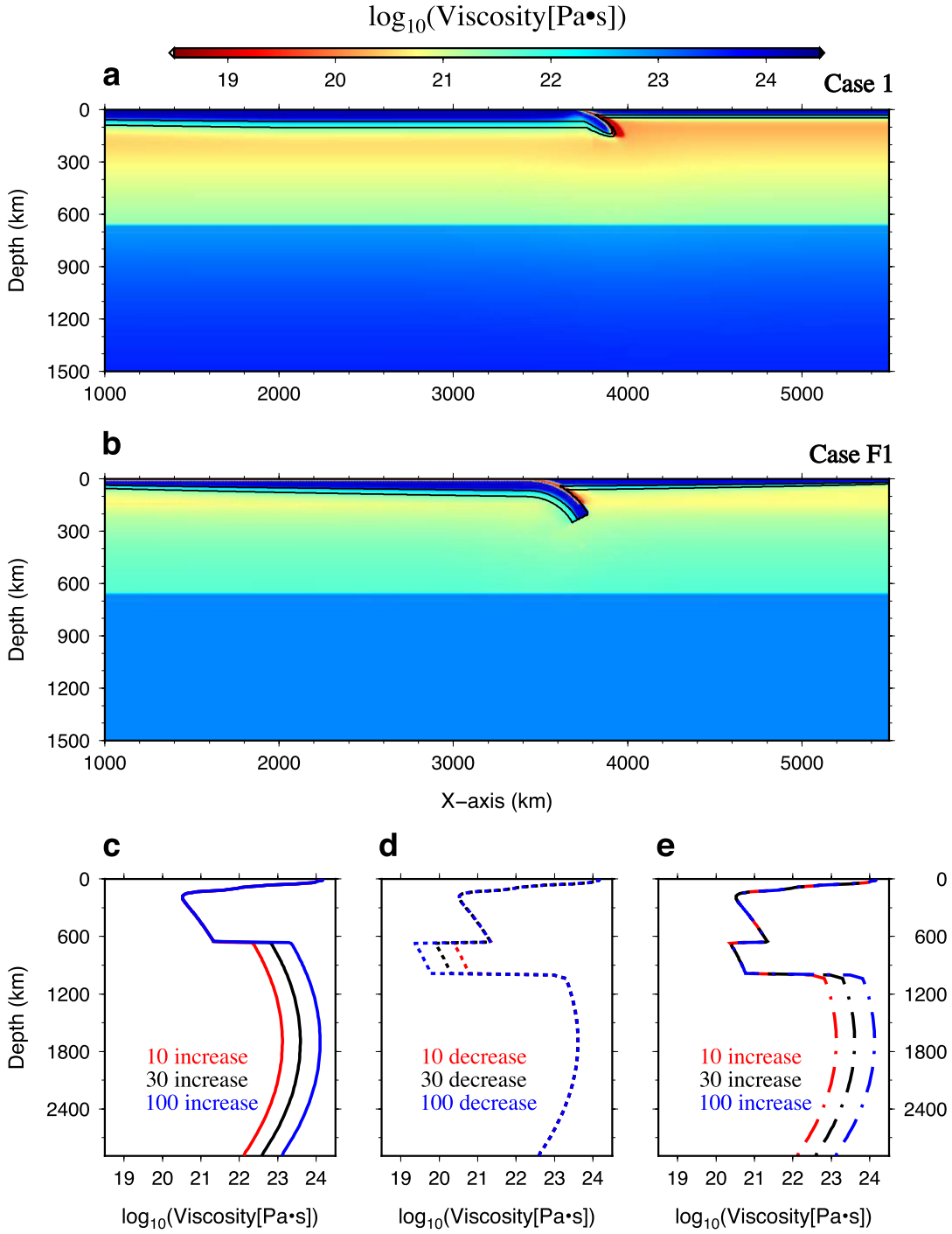

Figure 2. (a and b) Initial model setup for Case 1 and Case F1. Only part of the model domain is visualized here to highlight the plates. The black lines show the temperature contours of 800°C and 1,000°C, respectively. (c–e) Horizontally averaged viscosity structures for kinematic models. (c) Viscosity increases at 660 km depth are 10, 30, and 100 times, respectively. (d) Fix a viscosity increase of 30 times at 1,000 km depth, and change the viscosity decreases at 660 km depth from 10 times to 100 times. (e) Fix a reduction of 10 times in viscosity at 660 km depth, then increase the viscosity contrasts from 10 times to 100 times at 1,000 km depth. It is noted that all the viscosity jumps are relative to the upper mantle. The radial viscosity structures for fully dynamic models are shown in Figure S2.

Table 1
Model Parameters With Reference Values

Parameters	Values
Mantle thickness D	2,890 km
Surface thermal expansivity α_0	3×10^{-5} (°C)$^{-1}$
Surface thermal diffusivity κ_0	1×10^{-6} m^2/s
Surface density ρ_0	3,300 kg/m^3
Specific heat C_p	1,000 J/kg/K
Gravitational acceleration g	9.8 m/s^2
Surface temperature T_s	273 K
Temperature contrast $\triangle T$	1,350 K
Strain exponent n	3.0
Activation energy E	540 kJ/mol
Density jump for postspinel	9%
Density jump for Olivine—Wadsleyite	5%
Clapeyron slope of Olivine—Wadsleyite	2.7 MPa/K
Phase transition width of postspinel	30 km
Phase transition width of Olivine—Wadsleyite	30 km
λ_x, μ_x	30/10 km
λ_z, μ_z	150/10 km
Gravitational constant G	6.67×10^{-11} Nm^2/kg^2

The trench, located at 3,450 km horizontally, divides the subducting and overriding plates, which have lithospheric ages of (0.01–100) Myr and (0.01–40) Myr, respectively (Figure 2b). The initial temperature and mantle viscosity are the same as in the kinematic models except for the diffusion creep (Liu et al., 2021; McNamara et al., 2001; Turcotte & Schubert, 2014; Yang et al., 2018; Zhong & Gurnis, 1995):

$$\eta_{dif} = \eta_z \exp\left(\frac{E}{R_g} * \left(\frac{1}{T} - \frac{1}{T_r}\right) + E_c C\right), \quad (6)$$

where η_z is the viscosity with depth, R_g is the gas constant, E is the activation energy, T is the temperature, and T_r is the reference temperature (Figure S2). E_c controls the effective viscosity of a thin crust where C is the composition and varies from 0 to 1 (0: normal mantle; 1: weak oceanic crust). Here, a weak oceanic crust of 15 km at the top of the subducting plate is incorporated to decouple the subducting and overriding plates, and two weak ridges are applied to decouple the plates from the left and right boundaries. This simple strategy allows efficient computation of self-consistent models (Čížková & Bina, 2013; Holt et al., 2015; Yang et al., 2018). The viscosity reduction of the weak oceanic crustal layer is removed below a depth of 150 km (Figure 2b). All related parameters are presented in Table S1. The phase transitions at 410 and 660 km remain the same as in the kinematic model.

The top surface boundary conditions are determined either through imposing the top surface kinematics, or allowing the plate kinematics, including trench retreat, to be determined self-consistently. The velocity of an incoming plate, such as that for the Pacific, is determined by the sum of the forces around its periphery such using a fully self-consistent approach in 2D would overestimate the influence of the local slab. Consequently, we formulate models with each approach, but we find that final conclusions are independent of this assumption. Mechanically, the boundaries are free slip except for the surface where the subducting plate velocity and trench motion (overriding plate velocity) are prescribed kinematically allowing us to explore the role of surface plate motions and the presence of a LVC on slab dynamics (Christensen, 1996; Han & Gurnis, 1999; Liu et al., 2021; Yang et al., 2017). The surface boundary conditions are time-dependent since most subduction zones have undergone substantial trench rollback over the Cenozoic (e.g., Seton et al., 2012). This time-dependence is incorporated by simultaneously changing the position of the plate boundary of the surface velocity and the position of the weak-zone function. The surface and CMB temperatures are isothermal with values 0 and 1 nondimensionally, whereas the lateral boundaries are insulating.

The geoid and gravitational potential anomalies are solved as a linear sum of the internal density anomalies and the deflection of the top surface (e.g., McKenzie et al., 1974; Richards & Hager, 1984). The surface gravitational potential anomalies can be obtained by solving the Poisson equation $\nabla\phi = -2\pi G\delta\rho$, where G is the gravitational constant and $\delta\rho$ includes both internal density variations and that associated with surface dynamic topography. Here, the interior density anomaly is generally given by $\delta\rho = -\alpha_0\rho_0\delta T$, where α_0 is the thermal expansion coefficient, ρ_0 is the reference density, and δT is the temperature anomaly. The integration of the Poisson equation is calculated by using the Trapezoidal Rule (J. Chen & King, 1998) with the gravitational potential anomaly of a mass layer decaying exponentially with depth (Parker, 1972). The surface dynamic topography can be computed by $h = -\sigma_{zz} / \Delta\rho g$, where σ_{zz} is the total normal stress at the surface, $\Delta\rho$ is the density contrast across the surface, and g is the gravitational acceleration (e.g., Zhong et al., 2008). To avoid the topography associated with the tractions induced by prescribed plate motions, we resolve the Stokes equation with free-slip boundary condition (Davies, 1988). Self-gravitation is ignored, being unimportant at the wavelengths of slabs (Richards & Hager, 1984). The geoid is computed as ϕ / g. All related parameters can be found in Table 1.

Table 2
Parameters Setup for Different Models

Model	V_S (cm/yr)	V_T (cm/yr)	γ_{660} (MPa/K)	Viscosity contrast at 660 km depth	Viscosity contrast at 1,000 km depth	Subducting plate age (Myr)	Overriding plate age (Myr)
Case 1	6	−2	−1.5	30	No	100	20
Case 2	6	−2	−1.5	−10	30	100	20
Case 3	6	−2	−2.5	30	No	100	20
Case 4	6	−2	−3.5	30	No	100	20
Case 5	6	−2	−1.5	10	No	100	20
Case 6	6	−2	−2.5	10	No	100	20
Case 7	6	−2	−3.5	10	No	100	20
Case 8	6	−2	−1.5	100	No	100	20
Case 9	6	−2	−2.5	100	No	100	20
Case 10	6	−2	−3.5	100	No	100	20
Case 11	6	−2	−2.5	−10	30	100	20
Case 12	6	−2	−3.5	−10	30	100	20
Case 13	6	−2	−1.5	−30	30	100	20
Case 14	6	−2	−2.5	−30	30	100	20
Case 15	6	−2	−3.5	−30	30	100	20
Case 16	6	−2	−1.5	−100	30	100	20
Case 17	6	−2	−2.5	−100	30	100	20
Case 18	6	−2	−3.5	−100	30	100	20
Case 19	6	−2	−1.5	−10	10	100	20
Case 20	6	−2	−2.5	−10	10	100	20
Case 21	6	−2	−3.5	−10	10	100	20
Case 22	6	−2	−1.5	−10	100	100	20
Case 23	6	−2	−2.5	−10	100	100	20
Case 24	6	−2	−3.5	−10	100	100	20
Case 25	6	−2	−1.5	−10	30	40	20
Case 26	6	−2	−1.5	−10	30	70	20
Case 27	6	−2	−1.5	−10	30	100	50
Case 28	6	−2	−1.5	−10	30	100	80
Case 29	8	−2	−1.5	−10	30	100	20
Case 30	8	−3	−1.5	−10	30	100	20
Case 31	8	−4	−1.5	−10	30	100	20
Case 32	6	−3	−1.5	−10	30	100	20
Case 33	6	−4	−1.5	−10	30	100	20
Case 34*	6	−2	−1.5	−10	30	100	20
Case 35*	6	−2	−1.5	−10	30	100	20
Case F1			−1.5	30	No	0.01–100	0.01–40
Case F2			−1.5	−10	30	0.01–100	0.01–40
Case F3			−1.5	−30	30	0.01–100	0.01–40
Case F4			−1.5	−100	30	0.01–100	0.01–40

Abbreviations: V_S, Subducting plate velocity; V_T, Trench retreat velocity (overriding plate velocity); γ_{660}, Clapeyron slope of postspinel phase change; Case 34*, Consider metastable olivine phase change; Case 35*, Decrease reference viscosity from 3×10^{20} to 1×10^{20} Pa·s.

3. Result

The evolution of a slab with a viscosity increase of 30 times at 660 km depth (black line, Figure 2c) using the kinematic approach is shown (Figures 3a–3d, Movie S1). In this case, the slab descends through the upper mantle with a low dip angle (~42°), with buckling and folding as it reaches and interacts with the 660 km discontinuity. After a transient stagnation within the transition zone, it descends into the lower mantle slowly. The stress state within the cold core of the slab shows downdip compression once it comes into contact with the bottom of the mantle transition zone due to the combined resistance of the postspinel phase change and viscosity increase at 660 km discontinuity. The positive, long wavelength (>5,000 km) geoid increases over the slab as the slab evolves forward in time, reaching amplitudes of up to 30–40 m.

However, when we consider the LVC with a reduction in viscosity of 10 times at depths between 660 and 1,000 km relative to Case 1 (red dashed line, Figure 2d), the slab evolves with higher dip angle (~57°), and more easily penetrates into the lower mantle after ~15 Myr of convergence (Figures 3e–3f, Movie S2). Large amounts of slab become trapped within the LVC due to the viscosity reduction at 660 km followed by the jump at 1,000 km depth. With ongoing trench retreat, the slab has an even shorter period of transient stagnation in the mantle transition zone and descends quickly into the LVC. In addition, the slab is thinner in Case 2 throughout the mantle compared to Case 1 and is attributed to the decrease of resistance from the viscosity of the lower mantle (Figures 3e–3h, Movie S2). A rigid slab can be thought of as a stress guide, efficiently transmitting the positive buoyancy force from the endothermic postspinel phase change and viscosity increase between the upper and lower mantle to shallow depths. Thus, in this case, downdip tension occurs at shallow depth and at the top of the lower mantle due to the increase of an effective pull force at the uppermost lower mantle (Figures 3e–3h, Case 2). Furthermore, the positive long wavelength geoid height over slabs is far lower than that of Case 1, with an amplitude of only ~10 m. There are two components influencing the geoid resulting from the effects of the LVC (internal density and surface topography). Not only does the contribution arising from the slab temperature anomaly decrease but that from surface dynamic topography also decreases (Figure 4).

The influence of the LVC on the stress state within slabs is shown through the three groups of cases with variations of the strength of the postspinel phase change combined with the three kinds of viscosity structures (Figure 2, Cases 1–24 in Table 2). For each case, we first obtain the slab line that passes through the center of the cold core of the slab, then use *polyfit* (Engdahl et al., 1998) to fit the center line at depths between 70 and 350 km (Alpert et al., 2010). The slab dip angle is computed by taking the derivative of the polynomial at a depth and then use this dip to rotate the stress tensor into a slab coordinate system. Thus, the average force and dip angle along the slab core between depths from 100 to 300 km can be computed. The computations show that the LVC will increase the downdip tension of slabs at shallow depth substantially, especially when there is a small Clapeyron slope of postspinel (660 km) phase change and a large viscosity reduction at 660 km discontinuity, both of which reduce the upward buoyancy force on the slab at 660 km. In contrast, an increase in viscosity at either 660 km or 1,000 km will enlarge the downdip compression within slabs. Slabs, however, will be in tension unless the Clapeyron slope at 660 km depth is substantially more negative than −1.5 MPa/K (Figures 5a–5c). Besides, the average dip angles also vary with viscosity and Clapeyron slope (Figures 5d–5f). The LVC promotes the generation of high dip angles, which are at least ~10° larger than those without the LVC, and viscosity increases at 660 km or 1,000 km depth will decrease the subducting dip angles. The influence of the postspinel phase change is small unless its slope is large (e.g., −3.5 MPa/K) (Figures 5d–5f).

The long wavelength geoid is sensitive to the mantle viscosity structure, especially the relative viscosity contrasts between different layers (e.g., Hager & Richards, 1989). Thus, we first show the maximum long wavelength geoid height as a function of time for nine cases with a Clapeyron slope of −1.5 MPa/K corresponding to the three distinct viscosity structures (Figures 6a–6c). The long wavelength geoid high over slabs is only about ~10–15 m if there is a LVC (Figures 6b and 6c), in contrast, the geoid height is up to ~30–40 m in the presence of a viscosity jump at 660 km depth (Figure 6a). The detailed computations document how the postspinel phase transition and viscosity contrasts influence geoid height over slabs (Figures 6d–6f). We track the maximum long wavelength geoid between ~5 and ~45 Myr to avoid an initial transient after the start of subduction (Figure 6). The geoid high over the slab is most strongly controlled by viscosity jumps in the deep mantle with the influence of the postspinel phase change being secondary. A large viscosity jump

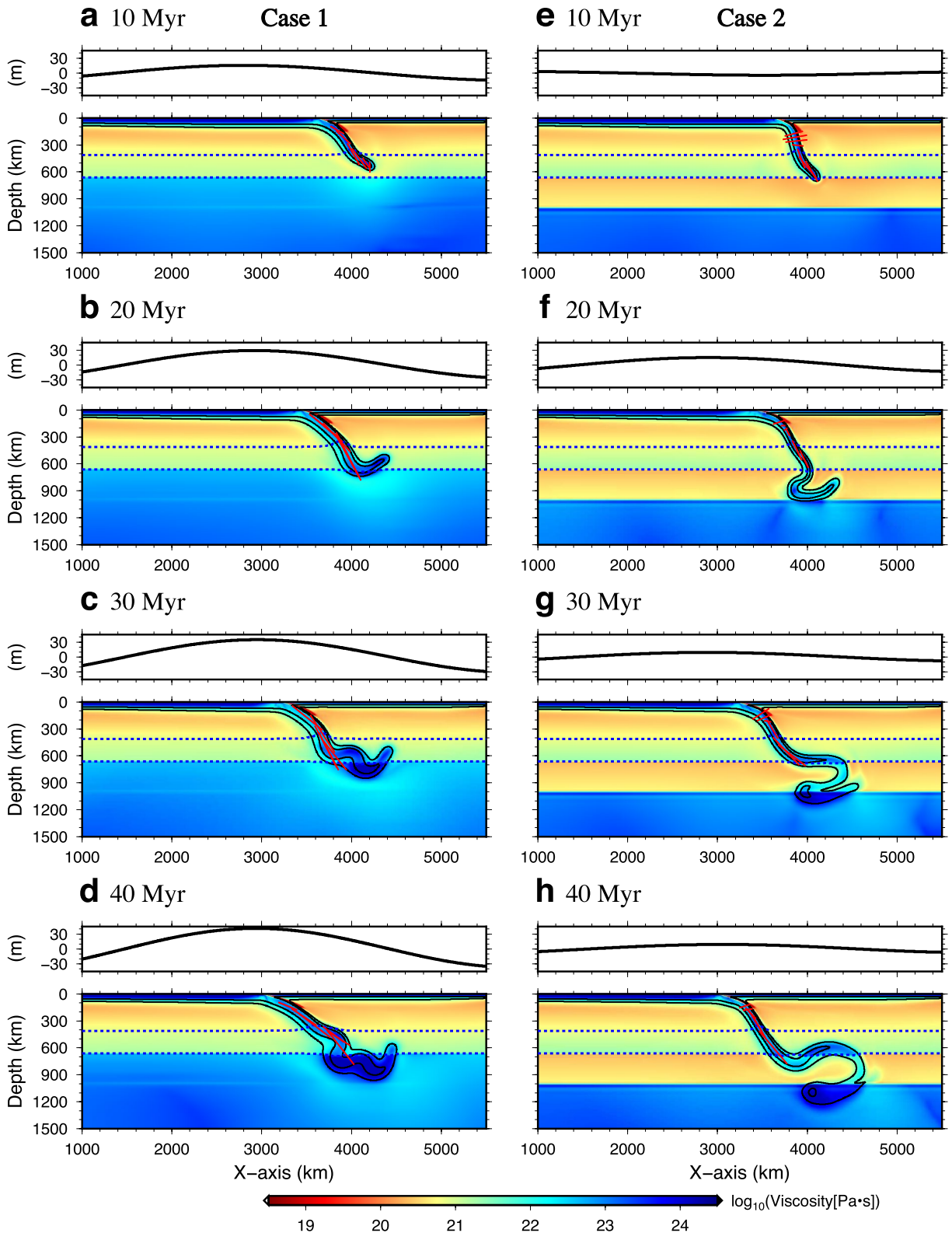

Figure 3. (a–d) The viscosity field and long wavelength geoid (wavelength is larger than 5,000 km) evolution for Case 1 and (e–h) the same for Case 2. These two viscosity structures correspond to the black solid line in Figure 2c and red dashed line in Figure 2d, respectively. The red bars represent the directions of principle compression stress along the slab cold core line. The black lines show the temperature contours of 800°C and 1,000°C, respectively.

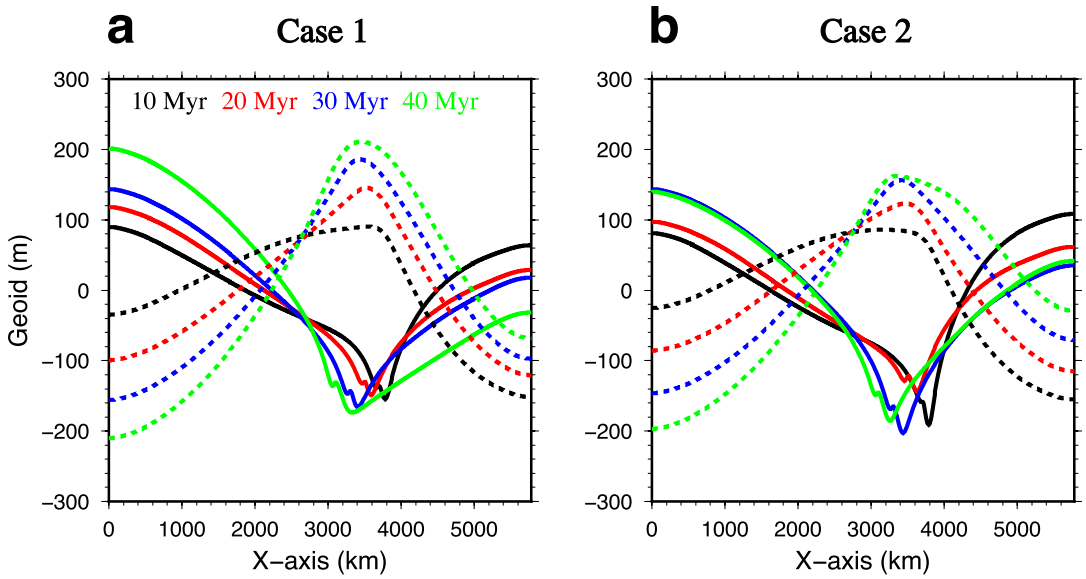

Figure 4. (a) Geoid components variations with time before filtering out short wavelengths (<~5,000 km) due to slab anomaly temperature (dashed lines) and surface dynamic topography (solid lines) for Case 1 and (b) the same for Case 2.

will increase the geoid high; moreover, the LVC will lower the geoid high substantially, reducing it to less than ~10 m (Figures 6d–6f).

The influences of the other parameters on stress state, dip angle, and geoid are further documented with additional calculations (Figure 7). Increasing subducting plate and overriding plate age will increase the downdip tension and downdip compression, respectively, whereas, they have a minor influence on the resulting geoid anomalies (Figures 7a and 7b). Larger plate subduction and trench retreat velocities will promote the generation of downdip compression within the slab and decrease the slab dip angle. The changes of convergence velocity cannot recover the observed long wavelength geoid highs over slabs (Figures 7c and 7d). Finally, the increased positive force derived from the metastable olivine phase change will strengthen the downdip compression within the slab and decrease the slab dip angle (Figure S1a) while decreasing the reference viscosity (from 3×10^{20} to 1×10^{20} Pa·s) has the opposite effect on stress state of slab (Figure S1b).

All of the above models described thus far used kinematic plate motions. Models with trench migration determined by the dynamics show that the transition in state-of-stress from compression throughout the slabs to downdip tension at shallow depth with the introduction of low viscosity channels below 660 km depth is unchanged. For models with dynamically evolving trench position, we start with Case F1 that has a viscosity increase of 30 times at 660 km depth (Figure 8, Movie S3 and Table 2). As in the corresponding cases for models with imposed trench motion, when the trench is free, the slab sinks and interacts with the transition zone, and stagnates horizontally for ~1,000 km in the transition zone. The stress state within the slab core changes from downdip tension at shallow depth to downdip compression throughout the slab as it evolves (Figures 8a–8d). We then compared this case with three additional cases where the viscosity decreases by 10, 30 and 100 times at 660 km depth along with an increase of 30 times at 1,000 km depth (Cases F2-F4, Table 2; Figures 8, S2, and S3; Movies S4–S6). With such viscosity structures, slabs easily penetrate into the lower mantle and become trapped in the LVC. Again, as with the models with trench motion imposed kinematically, all fully dynamic models show strong downdip tension between 100 and 400 km depths (Figures 8 and S3). The LVC not only lowers the geoid to ~10–15 m but also increases the trench retreat velocities substantially (Figures 8 and S4). The conclusion of the influence of radial mantle viscosity on slab state-of-stress is independent of the means by which trench motion is incorporated into models.

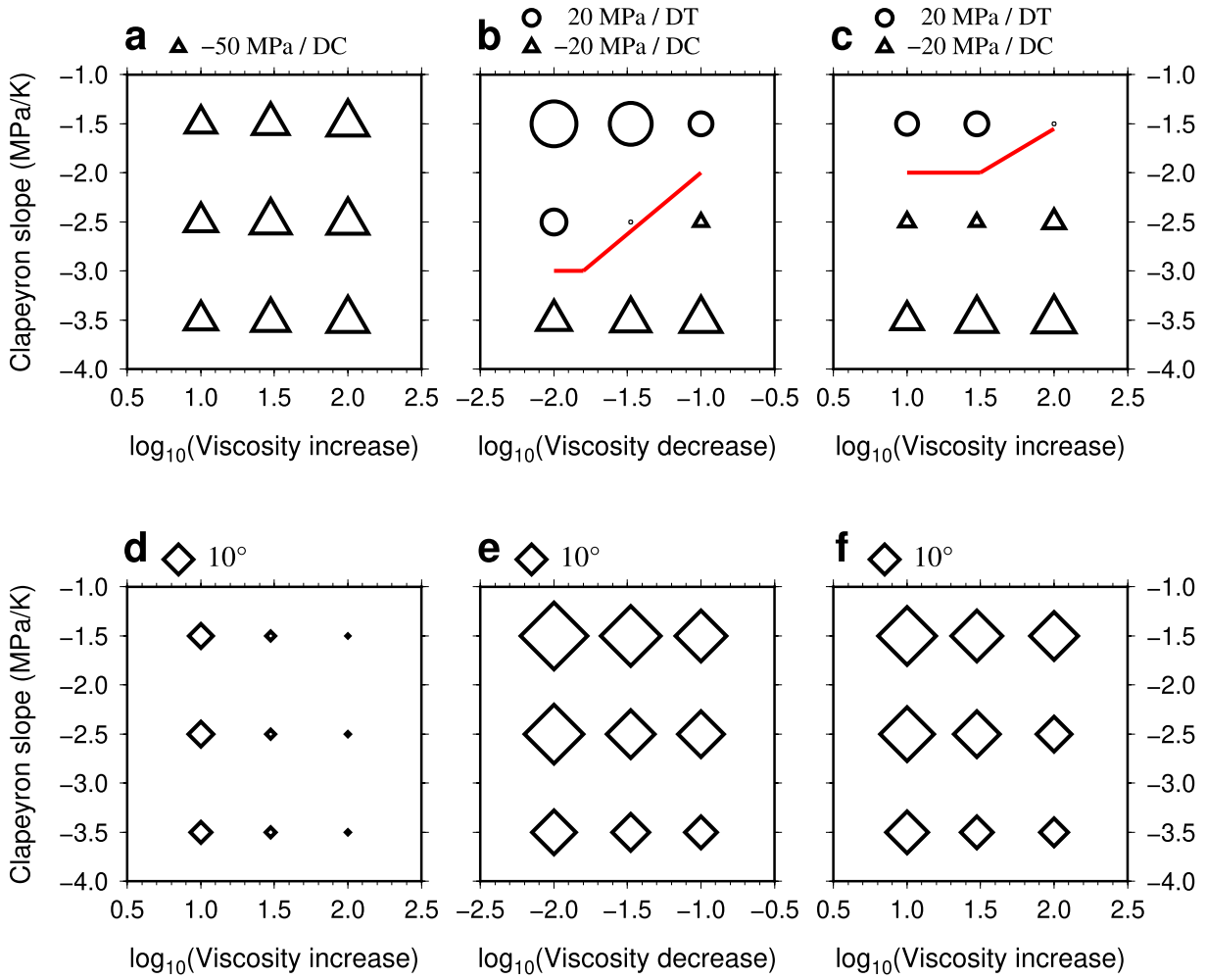

Figure 5. (a–c) Averaged force and (d–f) angle difference between actual dip angle and 40° along the slab cold core line at the depths between 100 and 300 km for each model in the diagrams of viscosity contrasts versus postspinel phase change. The three groups of viscosity structures in Figures 2c–2e correspond to the viscosity contrasts in each column, respectively (Negative represents reduction). DT: downdip tension; DC: downdip compression. The symbol area represents magnitude.

4. Discussion

The mantle viscosity structure has important implications for Earth's thermal and chemical evolution. Rudolph et al. (2015) used the long wavelength nonhydrostatic geoid and suggested that a low viscosity channel between 660 km and 1,000 km depths and a viscosity increase at ~1,000 km depth. Some previous studies also recovered similar viscosities, for example, Forte and Peltier (1991) proposed a two-layer viscous model with a jump of 9 times at 1,200 km based on matching the geoid, plate motions and core mantle boundary topography using a gravitationally consistent method. Moreover, the coexistence of two viscosity jumps at 670 and 1,022 km depths has been advanced in flow models that fit the observed geoid with three different *S*-wave tomographic models (King & Masters, 1992). Using a genetic algorithm and mantle convection models, Kido et al. (1998) were able to match the geoid at intermediate wavelengths (harmonic degrees 12–25) in different ocean basins (Atlantic, Indian, and Pacific Oceans) and argued for a low viscosity layer atop the lower mantle. Alternatively, Liu and Zhong (2016) used a Monte-Carlo approach with a thermal-chemical convection model to explore mantle viscosity and found that models with the viscosity increase at 660 km discontinuity can better fit the observed geoid than that with an increase at 1,000 km depth, in contrast to the Rudolph et al. (2015)'s result. Although assuming the depths (but not the contrast) of viscosity layers in flow models with plate boundaries, Yang and Gurnis (2016) found good fit to the long wavelength (degrees 2–8) geoid, free-air anomaly, gravity gradients, stress in the lithosphere

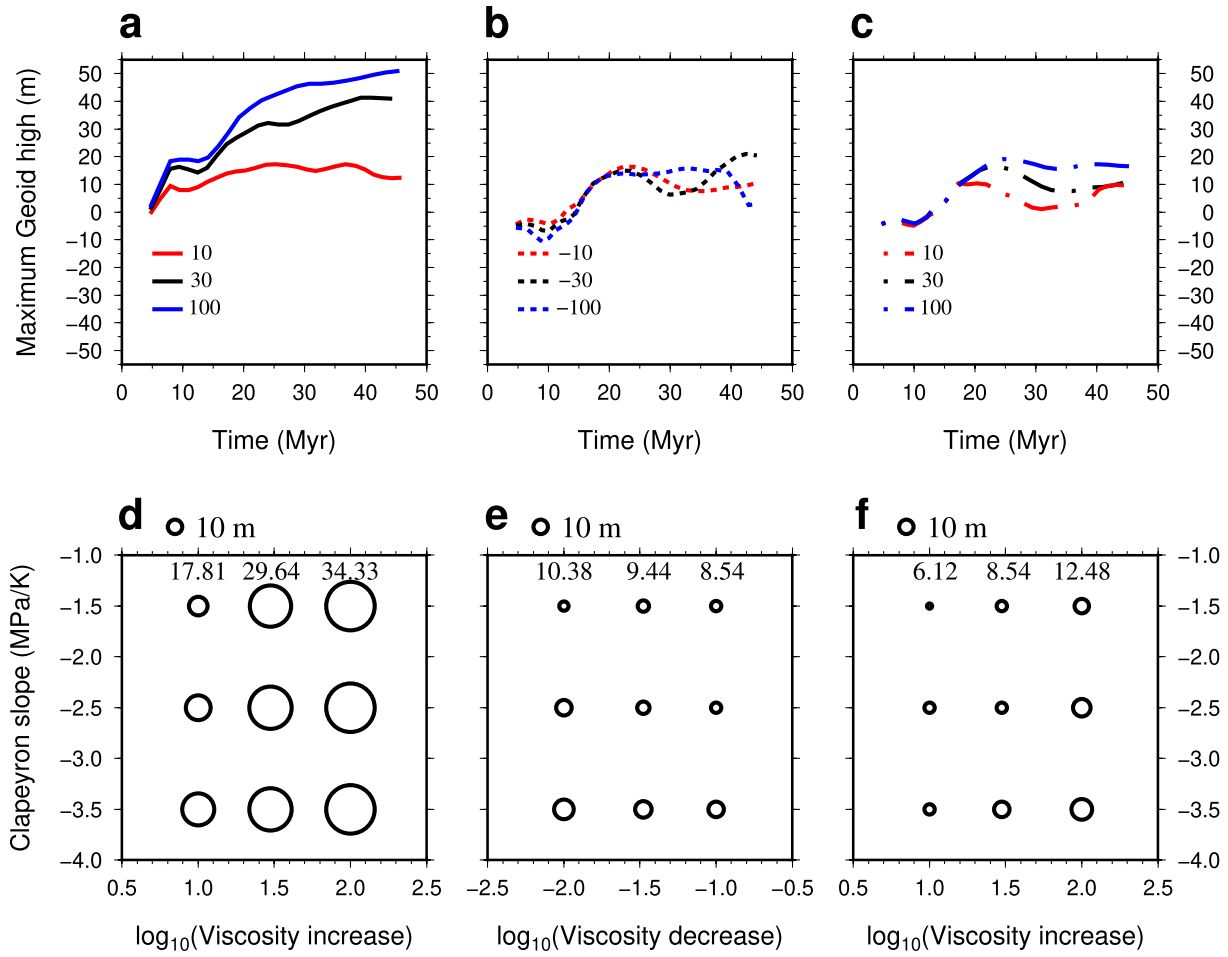

Figure 6. (a–c) Maximum long wavelength geoid variations with time corresponding to the three kinds of viscosity structures in Figure 2, respectively (a, Cases 1, 5, and 8; b, Cases 2, 13, and 16; c, Cases 2, 19, and 22. All the models have a Clapeyron slope of −1.5 MPa/K). (d–f) Averaged maximum long wavelength geoid since ~5 Myr for each model in the diagrams of viscosity contrasts (corresponding to the three different viscosity structures in Figure 2) versus postspinel phase change. In order to clearly show the effects of the viscosity contrasts on the geoid high over slab, we compute the averaged value for each column labeled at the top of each figure.

and high-accuracy residual topography. Moreover, Mao and Zhong (2021) conducted a global mantle convection model with plate motion history since the Cretaceous to produce mantle buoyancy and fit the observed geoid at degrees 4–12, supporting the hypothesis that the lower mantle viscosity is 30 times larger than that in the upper mantle. The longest wavelength (degrees 2–3) geoid is most sensitive to the viscosity contrasts and density anomalies in the lower mantle. However, in models that are capable of resolving shorter wavelength variations in viscosity, including those associated with subducting slabs, lateral variations have a large influence on the geoid (King, 2002; Moresi & Gurnis, 1996; Zhong & Davies, 1999; Zhong & Gurnis, 1992). Following earlier work that used models to fit the long wavelength geoid over slabs, we used time-dependent subduction models to determine the role of a low viscosity channel (LVC) at the top of the lower mantle. We find that the existence of the LVC will substantially decrease the amplitude of the long wavelength geoid over slabs making the signal inconsistent with the observed geoid (Figures 1 and 6).

Additional constraint on mantle viscosity variations comes from the focal mechanism of earthquakes within slabs. The principal axes orientations of CMT solutions can reflect the deformation state of slabs (e.g., P. F. Chen et al., 2004; Isacks & Molnar, 1969, 1971), which has been used to constrain the viscosity of slabs and the mantle using flow models (Billen et al., 2003; Carminati & Petricca, 2010; Gurnis & Hager, 1988; Vassiliou et al., 1984). Previous global analyses of focal mechanisms suggest that slabs in the western Pacific typically show downdip compression throughout, for example, Kurile, Izu-Bonin and Tonga, whereas

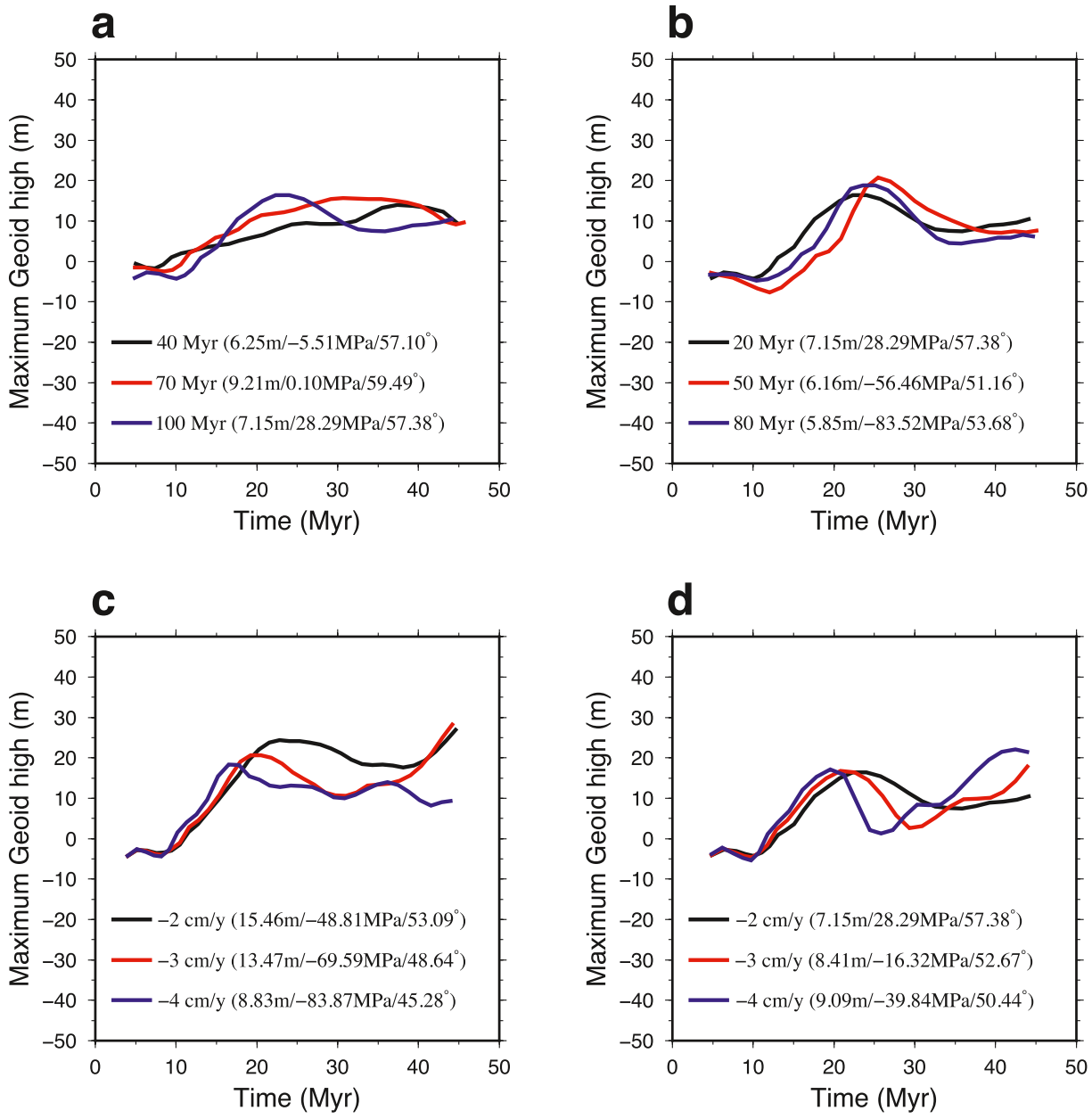

Figure 7. Maximum long wavelength geoid variations with time corresponding to the different plate ages and surface boundary conditions relative to the reference model (Case 2). (a) The subducting plate age changes from 40 to 100 Myr with the overriding plate age of 20 Myr (Cases 25 and 26). (b) The overriding plate age changes from 20 to 80 Myr with the subducting plate age of 100 Myr (Cases 27 and 28). (c, d) The trench retreat velocity changes from 2 to 4 cm/yr with the subducting plate velocities of 8 and 6 cm/yr, respectively (Cases 29–33). The averaged maximum long wavelength geoid, averaged force, and dip angle between 100 and 300 km depths since ~5 Myr are labeled in the figure for each model. Negative represents compression.

in the eastern Pacific, they typically show downdip tension at intermediate depth, for example, Chile, Peru (Alpert et al., 2010; Carminati & Petricca, 2010; Isacks & Molnar, 1971; Sandiford et al., 2020), although, slab deformation patterns are more complicated than either only downdip tension or downdip compression and many slabs display double seismic zones (DSZs) at intermediate depth with the upper part of the slab showing downdip compression and the lower part showing downdip tension, such as northern Japan, northern Tonga, and Chile (oppositely polarized DSZs) (Comte & Suarez, 1994; Kita et al., 2010; Wei et al., 2017). On the basis of the computed state-of-stress within the core of slabs, we find that the LVC will strengthen downdip tension in the upper 300 km conspicuously and is inconsistent with the deformation of slabs that are dominated by downdip compression in the western Pacific (Figure 5). Moreover, recent studies suggest

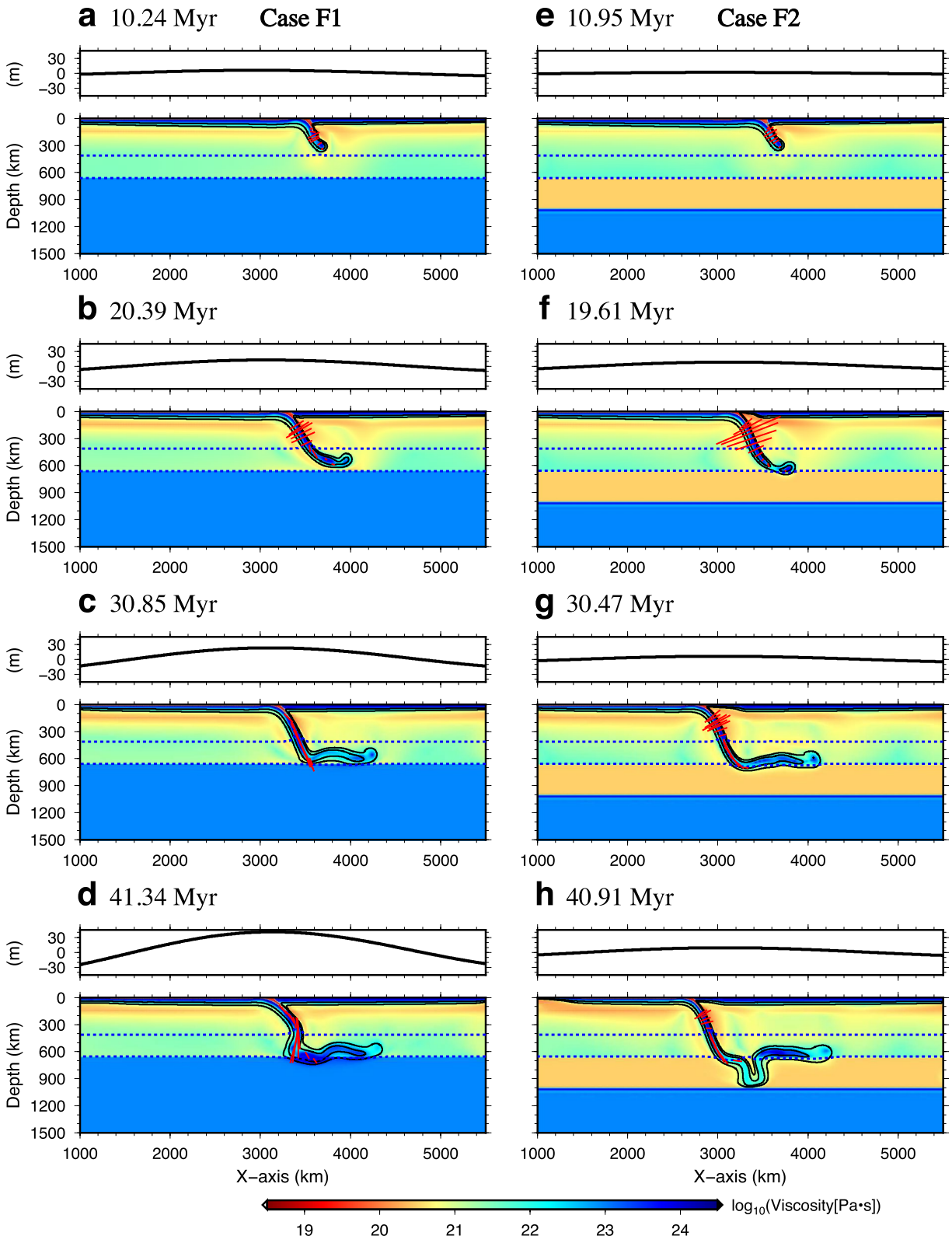

Figure 8. (a–d) Viscosity field and long wavelength geoid evolution for Case F1 and (e–h) the same for Case F2. These two viscosity structures correspond to the black and red lines in Figure S2, respectively. The red bars represent the directions of principle compression stress along the slab cold core.

that downdip tension seismicity in the Chilean, Peruvian, and Mexican flat slabs, strongly localized to the upper part of the subducting slabs, is controlled by an increase in curvature as the slab morphology changes from flattened to steep along strike (Sandiford et al., 2019, 2020). However, the LVC will increase the slab dip by 10–30° at the depths between 100 and 300 km (Figure 5), inhibiting the formation of a flat slab. Thus, the slab models with a LVC cannot fit the observed focal mechanisms globally.

Further evidence in support of a viscosity contrast at 1,000 km depth comes from interpretation of tomographic images, including inferred slab and plume deflections at this depth (French & Romanowicz, 2015; Fukao & Obayashi, 2013; Rudolph et al., 2015). However, more slabs evidently flatten in the mantle transition zone compared to 1,000 km depth (Fukao & Obayashi, 2013; Fukao et al., 2009; Goes et al., 2017). The largest horizontal slab in the transition zone occurs below east Asia, and Ma et al. (2019) show that close matches with seismic images can be obtained with a jump in viscosity of 30–50 times from upper mantle to lower mantle and a postspinel Clapeyron slope of −1.5 MPa/K with spherical convection models that explicitly incorporate the detailed plate kinematics of Asia and the Pacific. A recent review argues that the viscosity increase (20–50 times) between the upper and lower mantle, postspinel phase change (−1 to −2 MPa/K) and trench retreat are all necessary conditions to cause slabs to flatten within the mantle transition zone (Goes et al., 2017). Moreover, recent self-consistent mantle convection models show that if there is merely a viscosity jump at the depth of 1,000 km, then stagnation of subduction in the uppermost lower mantle will be absent, inconsistent with seismological observations (Wang & Li, 2020). Therefore, the observations of stagnated slabs seem to require both an increase in viscosity and a phase change near 660 km depth. In addition, some slabs appear to be approximately horizontal near a depth of 1,000 km (e.g., Kurile, Kermadec, and Indonesia). We do not know if it is a transient phase or long-term stagnation and its mechanism is not clear. With time-dependent inverse models that integrated plate kinematics, seismic images, basin subsidence, and surface state-of-stress, Yang et al. (2016) argued that the large seismic anomaly above 1,000 km depth below Indonesia was a relic of a previous horizontal slab at 660 km depth that has been slowly falling into the lower mantle. The initial descent of that horizonal slab into the lower mantle induced surface subsidence and compression during the Miocene. Alternatively, Ballmer et al. (2015) suggest that compositional mantle layering can render slabs neutrally buoyant at the top of the lower mantle. Other factors will require additional work, including trench retreat velocity and the history of subduction. However, integrating slab state-of-stress, as we have done, in models that also match a variety of time-dependent surface observations (e.g., Yang et al., 2016) could resolve the uncertainty associated with estimates of mantle viscosity within the transition zone.

5. Conclusion

We develop a series of dynamic models to investigate the effects of mantle viscosity on slabs that are compared against geophysical observations. We find that the LVC will substantially lower the long wavelength geoid height over slabs, reducing it to only ∼10 m, while increasing the slab dip angle and the downdip tension within slabs at depths shallower than 300 km. A jump in viscosity at 660 km depth produces strong downdip compression throughout a slab, an outcome that will largely disappear when there is a LVC. The LVC between 660 and 1,000 km depths is not compatible with the observed long wavelength geoid and focal mechanism. Our results support a viscosity increase of ∼30–100 times at the 660 km discontinuity and have significant implications for interpretation of seismic tomography and the thermochemical evolution of the mantle.

Acknowledgments
Hao Liu's visit to Caltech was supported by the Strategic Priority Research Program of Chinese Academy of Sciences, Grant No. XDB 41000000 and the China Scholarship Council. Additional support provided by the National Science Foundation through awards EAR-1645775 and EAR-2009935, and National Natural Science Foundation of China (41774105 and 41820104004). Some of the computations carried out on the NSF XSEDE systems, made possible by TG-EAR160027. The authors acknowledge the advice from Wei Mao, Ting Yang, and Jiayan Tan.

Data Availability Statement

The mantle convection code Citcom is available at the website https://geodynamics.org/cig/, while model data files will be available at https://data.caltech.edu/.

References

Agrusta, R., Goes, S., & Van Hunen, J. (2017). Subducting-slab transition-zone interaction: Stagnation, penetration and mode switches. *Earth and Planetary Science Letters*, *464*, 10–23. https://doi.org/10.1016/j.epsl.2017.02.005

Alpert, L. A., Becker, T. W., & Bailey, I. W. (2010). Global slab deformation and centroid moment tensor constraints on viscosity. *Geochemistry, Geophysics, Geosystems*, *11*(12). https://doi.org/10.1029/2010GC003301

Ballmer, M. D., Schmerr, N. C., Nakagawa, T., & Ritsema, J. (2015). Compositional mantle layering revealed by slab stagnation at ~1000-km depth. *Science Advances*, *1*, e1500815. https://doi.org/10.1126/sciadv.1500815

Billen, M. I. (2020). Deep slab seismicity limited by rate of deformation in the transition zone. *Science Advances*, *6*, eaaz7692. https://doi.org/10.1126/sciadv.aaz7692

Billen, M. I., Gurnis, M., & Simons, M. (2003). Multiscale dynamics of the Tonga—Kermadec subduction zone. *Geophysical Journal International*, *153*(2), 359–388. https://doi.org/10.1046/j.1365-246x.2003.01915.x

Bower, D. J., Gurnis, M., & Flament, N. (2015). Assimilating lithosphere and slab history in 4-D Earth models. *Physics of the Earth and Planetary Interiors*, *238*, 8–22. https://doi.org/10.1016/j.pepi.2014.10.013

Carminati, E., & Petricca, P. (2010). State of stress in slabs as a function of large-scale plate kinematics. *Geochemistry, Geophysics, Geosystems*, *11*(4). https://doi.org/10.1029/2009GC003003

Chen, J., & King, S. D. (1998). The influence of temperature and depth dependent viscosity on geoid and topography profiles from models of mantle convection. *Physics of the Earth and Planetary Interiors*, *106*(1–2), 75–92. https://doi.org/10.1016/s0031-9201(97)00110-6

Chen, P. F., Bina, C. R., & Okal, E. A. (2004). A global survey of stress orientations in subducting slabs as revealed by intermediate-depth earthquakes. *Geophysical Journal International*, *159*(2), 721–733. https://doi.org/10.1111/j.1365-246x.2004.02450.x

Christensen, U. R. (1996). The influence of trench migration on slab penetration into the lower mantle. *Earth and Planetary Science Letters*, *140*(1–4), 27–39. https://doi.org/10.1016/0012-821x(96)00023-4

Christensen, U. R., & Yuen, D. A. (1985). Layered convection induced by phase transitions. *Journal of Geophysical Research*, *90*(B12), 10291–10300. https://doi.org/10.1029/jb090ib12p10291

Čížková, H., & Bina, C. R. (2013). Effects of mantle and subduction-interface rheologies on slab stagnation and trench rollback. *Earth and Planetary Science Letters*, *379*, 95–103.

Comte, D., & Suarez, G. (1994). An inverted double seismic zone in Chile: Evidence of phase transformation in the subducted slab. *Science*, *263*(5144), 212–215. https://doi.org/10.1126/science.263.5144.212

Davies, G. F. (1988). Role of the lithosphere in mantle convection. *Journal of Geophysical Research*, *93*(B9), 10451–10466. https://doi.org/10.1029/jb093ib09p10451

Engdahl, E. R., van der Hilst, R., & Buland, R. (1998). Global teleseismic earthquake relocation with improved travel times and procedures for depth determination. *Bulletin of the Seismological Society of America*, *88*(3), 722–743.

Forte, A. M., & Peltier, R. (1991). Viscous flow models of global geophysical observables: 1. Forward problems. *Journal of Geophysical Research*, *96*(B12), 20131–20159. https://doi.org/10.1029/91JB01709

Forte, A. M., Simmons, N. A., & Grand, S. P. (2015). Constraints on seismic models from other disciplines––Constraints on 3-D seismic models from global geodynamic observables: Implications for the global mantle convective flow. In G. Schubert (Ed.), *Treatise on geophysics* (2nd ed., pp. 853–907). Elsevier. https://doi.org/10.1016/B978-0-444-53802-4.00028-2

French, S. W., & Romanowicz, B. (2015). Broad plumes rooted at the base of the Earth's mantle beneath major hotspots. *Nature*, *525*(7567), 95–99. https://doi.org/10.1038/nature14876

Fukao, Y., & Obayashi, M. (2013). Subducted slabs stagnant above, penetrating through, and trapped below the 660 km discontinuity. *Journal of Geophysical Research: Solid Earth*, *118*, 5920–5938. https://doi.org/10.1002/2013JB010466

Fukao, Y., Obayashi, M., Nakakuki, T., & Deep Slab Project Group. (2009). Stagnant slab: A review. *Annual Review of Earth and Planetary Sciences*, *37*, 19–46. https://doi.org/10.1146/annurev.earth.36.031207.124224

Ghosh, A., Becker, T. W., & Zhong, S. J. (2010). Effects of lateral viscosity variations on the geoid. *Geophysical Research Letters*, *37*, L01301. https://doi.org/10.1029/2009GL040426

Goes, S., Agrusta, R., van Hunen, J., & Garel, F. (2017). Subduction-transition zone interaction: A review. *Geosphere*, *13*(3), 644–664. https://doi.org/10.1130/ges01476.1

Grima, A. G., Lithgow-Bertelloni, C., & Crameri, F. (2020). Orphaning Regimes: The missing link between flattened and penetrating slab morphologies. *Frontiers of Earth Science*, *8*, L01301. https://doi.org/10.3389/feart.2020.00374

Gurnis, M., & Hager, B. H. (1988). Controls of the structure of subducted slabs. *Nature*, *335*(6188), 317–321. https://doi.org/10.1038/335317a0

Hager, B. H. (1984). Subducted slabs and the geoid: Constraints on mantle rheology and flow. *Journal of Geophysical Research*, *89*(B7), 6003–6015. https://doi.org/10.1029/jb089ib07p06003

Hager, B. H., & Richards, M. A. (1989). Long-wavelength variations in Earth's geoid: Physical models and dynamical implications. *Philosophical Transactions of the Royal Society of London—Series A: Mathematical and Physical Sciences*, *328*(1599), 309–327. https://doi.org/10.1098/rsta.1989.0038

Han, L., & Gurnis, M. (1999). How valid are dynamic models of subduction and convection when plate motions are prescribed? *Physics of the Earth and Planetary Interiors*, *110*(3–4), 235–246. https://doi.org/10.1016/s0031-9201(98)00156-3

Hayes, G. P., Wald, D. J., & Johnson, R. L. (2012). Slab1.0: A three-dimensional model of global subduction zone geometries. *Journal of Geophysical Research*, *117*(B1). https://doi.org/10.1029/2011JB008524

Hirth, G., & Kohlstedf, D. (2003). Rheology of the upper mantle and the mantle wedge: A view from the experimentalists. *Geophysical Monograph-American Geophysical Union*, *138*, 83–105. https://doi.org/10.1029/138gm06

Holt, A. F., Becker, T. W., & Buffett, B. A. (2015). Trench migration and overriding plate stress in dynamic subduction models. *Geophysical Journal International*, *201*(1), 172–192. https://doi.org/10.1093/gji/ggv011

Homrighausen, S., Hoernle, K., Zhou, H., Geldmacher, J., Wartho, J. A., Hauff, F. (2020). Paired EMI-HIMU hotspots in the South Atlantic—Starting plume heads trigger compositionally distinct secondary plumes? *Science Advances*, *6*, eaba0282. https://doi.org/10.1126/sciadv.aba0282

Isacks, B., & Molnar, P. (1969). Mantle earthquake mechanisms and the sinking of the lithosphere. *Nature*, *223*(5211), 1121–1124. https://doi.org/10.1038/2231121a0

Isacks, B., & Molnar, P. (1971). Distribution of stresses in the descending lithosphere from a global survey of focal-mechanism solutions of mantle earthquakes. *Reviews of Geophysics*, *9*(1), 103–174. https://doi.org/10.1029/rg009i001p00103

Karato, S. I. (2008). *Deformation of Earth materials*. An Introduction to the Rheology of Solid Earth (463). Cambridge University Press. https://doi.org/10.1017/cbo9780511804892

Kido, M., Yuen, D. A., Čadek, O., & Nakakuki, T. (1998). Mantle viscosity derived by genetic algorithm using oceanic geoid and seismic tomography for whole-mantle versus blocked-flow situations. *Physics of the Earth and Planetary Interiors*, *107*(4), 307–326. https://doi.org/10.1016/s0031-9201(98)00077-6

King, S. D. (1995). The viscosity structure of the mantle. *Reviews of Geophysics*, *33*(S1), 11–17. https://doi.org/10.1029/95rg00279

King, S. D. (2002). Geoid and topography over subduction zones: The effect of phase transformations. *Journal of Geophysical Research*, *107*(B1), ETG 2-1–ETP 2-10. https://doi.org/10.1029/2000JB000141

King, S. D. (2016). An evolving view of transition zone and midmantle viscosity. *Geochemistry, Geophysics, Geosystems*, *17*, 1234–1237. https://doi.org/10.1002/2016GC006279

King, S. D., & Masters, G. (1992). An inversion for radial viscosity structure using seismic tomography. *Geophysical Research Letters*, *19*, 1551–1554. https://doi.org/10.1029/92GL01700

Kita, S., Okada, T., Hasegawa, A., Nakajima, J., & Matsuzawa, T. (2010). Existence of interplane earthquakes and neutral stress boundary between the upper and lower planes of the double seismic zone beneath Tohoku and Hokkaido, northeastern Japan. *Tectonophysics*, *496*(1–4), 68–82. https://doi.org/10.1016/j.tecto.2010.10.010

Lemoine, F. G., Smith, D. E., Kunz, L., Smith, R., Pavlis, E. C., Pavlis, N. K., et al. (1997). The development of the NASA GSFC and NIMA joint geopotential model. In *Gravity, geoid and marine geodesy* (pp. 461–469). Springer. https://doi.org/10.1007/978-3-662-03482-8_62

Leng, W., & Gurnis, M. (2012). Shape of thermal plumes in a compressible mantle with depth-dependent viscosity. *Geophysical Research Letters*, *39*, L05310. https://doi.org/10.1029/2012GL050959

Li, Z. H., Gerya, T., & Connolly, J. A. (2019). Variability of subducting slab morphologies in the mantle transition zone: Insight from petrological-thermomechanical modeling. *Earth-Science Reviews*, *196*, 102874. https://doi.org/10.1016/j.earscirev.2019.05.018

Liu, H., Gurnis, M., Leng, W., Jia, Z., & Zhan, Z. (2021). Tonga slab morphology and stress variations controlled by a relic slab: Implications for deep earthquakes in the Tonga-Fiji Region. *Geophysical Research Letters*, *48*, e2020GL091331. https://doi.org/10.1029/2020GL091331

Liu, H., & Leng, W. (2020). Plume-tree structure induced by low-viscosity layers in the upper mantle. *Geophysical Research Letters*, *47*, e2019GL086508. https://doi.org/10.1029/2019GL086508

Liu, H., Wang, W., Jia, X., Leng, W., Wu, Z., & Sun, D. (2018). The combined effects of post-spinel and post-garnet phase transitions on mantle plume dynamics. *Earth and Planetary Science Letters*, *496*, 80–88. https://doi.org/10.1016/j.epsl.2018.05.031

Liu, X., & Zhong, S. (2016). Constraining mantle viscosity structure for a thermochemical mantle using the geoid observation. *Geochemistry, Geophysics, Geosystems*, *17*, 895–913. https://doi.org/10.1002/2015GC006161

Ma, P., Liu, S., Gurnis, M., & Zhang, B. (2019). Slab horizontal subduction and slab tearing beneath East Asia. *Geophysical Research Letters*, *46*, 5161–5169. https://doi.org/10.1029/2018GL081703

Mao, W., & Zhong, S. (2018). Slab stagnation due to a reduced viscosity layer beneath the mantle transition zone. *Nature Geoscience*, *11*(11), 876–881. https://doi.org/10.1038/s41561-018-0225-2

Mao, W., & Zhong, S. (2021). Constraints on mantle viscosity from intermediate-wavelength geoid anomalies in mantle convection models with plate motion history. *Journal of Geophysical Research: Solid Earth*, *126*, e2020JB021561. https://doi.org/10.1029/2020JB021561

McKenzie, D. P., Roberts, J. M., & Weiss, N. O. (1974). Convection in the earth's mantle: Towards a numerical simulation. *Journal of Fluid Mechanics*, *62*, 465–538.

McNamara, A. K., Karato, S. I., & Van Keken, P. E. (2001). Localization of dislocation creep in the lower mantle: Implications for the origin of seismic anisotropy. *Earth and Planetary Science Letters*, *191*(1–2), 85–99. https://doi.org/10.1016/s0012-821x(01)00405-8

Mitrovica, J. X., & Forte, A. M. (2004). A new inference of mantle viscosity based upon joint inversion of convection and glacial isostatic adjustment data. *Earth and Planetary Science Letters*, *225*(1–2), 177–189. https://doi.org/10.1016/j.epsl.2004.06.005

Moresi, L., & Gurnis, M. (1996). Constraints on the lateral strength of slabs from three-dimensional dynamic flow models. *Earth and Planetary Science Letters*, *138*(1–4), 15–28. https://doi.org/10.1016/0012-821x(95)00221-w

Moresi, L., Zhong, S., & Gurnis, M. (1996). The accuracy of finite element solutions of Stokes's flow with strongly varying viscosity. *Physics of the Earth and Planetary Interiors*, *97*, 83–94. https://doi.org/10.1016/0031-9201(96)03163-9

Panasyuk, S. V., & Hager, B. H. (1998). A model of transformational superplasticity in the upper mantle. *Geophysical Journal International*, *133*(3), 741–755. https://doi.org/10.1046/j.1365-246x.1998.00539.x

Parker, R. L. (1972). The rapid calculation of potential anomalies. *Geophysical Journal of Royal Astronomical Society*, *31*, 447–455.

Richards, M. A., & Hager, B. H. (1984). Geoid anomalies in a dynamic Earth. *Journal of Geophysical Research*, *89*(B7), 5987–6002. https://doi.org/10.1029/jb089ib07p05987

Richards, M. A., & Hager, B. H. (1989). Effects of lateral viscosity variations on long-wavelength geoid anomalies and topography. *Journal of Geophysical Research*, *94*(B8), 10299–10313. https://doi.org/10.1029/jb094ib08p10299

Rudolph, M. L., Lekić, V., & Lithgow-Bertelloni, C. (2015). Viscosity jump in Earth's mid-mantle. *Science*, *350*(6266), 1349–1352. https://doi.org/10.1126/science.aad1929

Sandiford, D., Moresi, L., Sandiford, M., & Yang, T. (2019). Geometric controls on flat slab seismicity. *Earth and Planetary Science Letters*, *527*, 115787. https://doi.org/10.1016/j.epsl.2019.115787

Sandiford, D., Moresi, L. M., Sandiford, M., Farrington, R., & Yang, T. (2020). The fingerprints of flexure in slab seismicity. *Tectonics*, *39*(8), e2019TC005894. https://doi.org/10.1029/2019TC005894

Schmeling, H., Monz, R., & Rubie, D. C. (1999). The influence of olivine metastability on the dynamics of subduction. *Earth and Planetary Science Letters*, *165*(1), 55–66. https://doi.org/10.1016/s0012-821x(98)00249-0

Seton, M., Müller, R. D., Zahirovic, S., Gaina, C., Torsvik, T., Shephard, G., et al. (2012). Global continental and ocean basin reconstructions since 200 Ma. *Earth-Science Reviews*, *113*(3–4), 212–270. https://doi.org/10.1016/j.earscirev.2012.03.002

Tosi, N., Čadek, O., & Martinec, Z. (2009). Subducted slabs and lateral viscosity variations: Effects on the long-wavelength geoid. *Geophysical Journal International*, *179*(2), 813–826. https://doi.org/10.1111/j.1365-246x.2009.04335.x

Turcotte, D., & Schubert, G. (2014). *Geodynamics*. Cambridge University Press.

Vassiliou, M. S., Hager, B. H., & Raefsky, A. (1984). The distribution of earthquakes with depth and stress in subducting slabs. *Journal of Geodynamics*, *1*(1), 11–28. https://doi.org/10.1016/0264-3707(84)90004-8

Wang, Y., & Li, M. (2020). Constraining mantle viscosity structure from a statistical analysis of slab stagnation events. *Geochemistry, Geophysics, Geosystems*, *21*, e2020GC009286. https://doi.org/10.1029/2020GC009286

Wei, S. S., Wiens, D. A., van Keken, P. E., & Cai, C. (2017). Slab temperature controls on the Tonga double seismic zone and slab mantle dehydration. *Science advances*, *3*, e1601755. https://doi.org/10.1126/sciadv.1601755

Yang, T., & Gurnis, M. (2016). Dynamic topography, gravity and the role of lateral viscosity variations from inversion of global mantle flow. *Geophysical Supplements to the Monthly Notices of the Royal Astronomical Society*, *207*(2), 1186–1202. https://doi.org/10.1093/gji/ggw335

Yang, T., Gurnis, M., & Zahirovic, S. (2016). Mantle-induced subsidence and compression in SE Asia since the early Miocene. *Geophysical Research Letters*, *43*, 1901–1909. https://doi.org/10.1002/2016GL068050

Yang, T., Gurnis, M., & Zahirovic, S. (2018). Slab avalanche-induced tectonics in self-consistent dynamic models. *Tectonophysics*, *746*, 251–265. https://doi.org/10.1016/j.tecto.2016.12.007

Yang, T., Gurnis, M., & Zhan, Z. (2017). Trench motion-controlled slab morphology and stress variations: Implications for the isolated 2015 Bonin Islands deep earthquake. *Geophysical Research Letters*, *44*(13), 6641–6650. https://doi.org/10.1002/2017GL073989

Yoshida, M., & Nakakuki, T. (2009). Effects on the long-wavelength geoid anomaly of lateral viscosity variations caused by stiff subducting slabs, weak plate margins and lower mantle rheology. *Physics of the Earth and Planetary Interiors*, *172*(3–4), 278–288. https://doi.org/10.1016/j.pepi.2008.10.018

Zhang, S., & Christensen, U. (1993). Some effects of lateral viscosity variations on geoid and surface velocities induced by density anomalies in the mantle. *Geophysical Journal International*, *114*(3), 531–547. https://doi.org/10.1111/j.1365-246x.1993.tb06985.x

Zhong, S. (2006). Constraints on thermochemical convection of the mantle from plume heat flux, plume excess temperature, and upper mantle temperature. *Journal of Geophysical Research*, *111*(B4). https://doi.org/10.1029/2005JB003972

Zhong, S., & Davies, G. F. (1999). Effects of plate and slab viscosities on the geoid. *Earth and Planetary Science Letters*, *170*(4), 487–496. https://doi.org/10.1016/s0012-821x(99)00124-7

Zhong, S., & Gurnis, M. (1992). Viscous flow model of a subduction zone with a faulted lithosphere: Long and short wavelength topography, gravity and geoid. *Geophysical Research Letters*, *19*(18), 1891–1894. https://doi.org/10.1029/92GL02142

Zhong, S., & Gurnis, M. (1995). Mantle convection with plates and mobile, faulted plate margins. *Science*, *267*(5199), 838–843. https://doi.org/10.1126/science.267.5199.838

Zhong, S., McNamara, A., Tan, E., Moresi, L., & Gurnis, M. (2008). A benchmark study on mantle convection in a 3-D spherical shell using CitcomS. *Geochemistry, Geophysics, Geosystems*, *9*(10). https://doi.org/10.1029/2008GC002048